Icarus 208 (2010) 395–401

Contents lists available at ScienceDirect

Icarus

journal homepage: www.elsevier.com/locate/icarus

Sizes, shapes, and derived properties of the saturnian satellites after the Cassini nominal mission

P.C. Thomas

Center for Radiophysics and Space Research, Cornell University, Ithaca, NY 14853, USA

ARTICLE INFO

Article history:
Received 1 October 2009
Revised 14 January 2010
Accepted 24 January 2010
Available online 4 February 2010

Keywords:
Saturn, Satellites
Geophysics
Geological processes

ABSTRACT

The Cassini spacecraft has provided data on over twenty satellites orbiting Saturn. In this study we update the shape measurements derived from imaging data of nearly all the observed regular satellites (those with low eccentricities and inclinations) and briefly discuss some of the implications of their properties. In particular, the improved data show that Rhea's shape is hydrostatic.

1. Introduction and methods

Knowledge of the shapes and sizes of satellites is crucial for determining their mean densities, making geophysical interpretations, and producing maps. The 4-year nominal mission of the Cassini spacecraft has now provided data on more than 20 satellites. This work updates most of the previously published shapes and sizes, and briefly reviews some of the newer shape-related interpretations. The larger ellipsoidal satellites have been imaged multiple times both during "targeted" flybys which are less than a few thousand kilometers, and more often during other opportunities typically at a few hundred thousand kilometer range. The smaller satellites, excepting Phoebe, have been seen close-up at irregular intervals as the spacecraft orbit and data taking allow. Phoebe was seen in detail for more than one rotation as the Cassini spacecraft passed by on its way to Saturn. The other outer, small satellites are too small and too distant to resolve from the Cassini orbits.

The shapes and sizes of ellipsoidal satellites are primarily measured by limb coordinates in the Imaging Science Subsystem (ISS) data (Porco et al., 2004). The measurement techniques are described in Thomas et al. (1998, 2007a). These involve sub-pixel modeling of the bright edge of an illuminated object. Precisions of limb coordinate measurements, that is, the reproducibility of the image plane coordinates around the limb, can reach better than 0.1 pixels. Accuracies, checked by images of greatly differing resolutions or with independent data, can approach 0.15 pixels. Pixel scale uncertainties are generally 10^{-4} or better (a few kilometers out of >100,000 km) and do not materially affect the measured sizes. The solutions for shapes are affected by how well an ellipse center is fit for each view; the rougher the object or the shorter the limb arc, the less accurate is the calculated center and the less accurate the overall ellipsoidal solution. Views with more than 180° of limb arc, such as transits of the satellite in front of Saturn, those at very low phase, or those with Saturn shine are valuable in that they can set particular projected diameters with very high accuracy and thereby help stabilize the fit centers of all other views. The geometry of projected limbs of ellipsoids is described in detail in Dermott and Thomas (1988). Stereogrammetric control point solutions are used to verify some aspects of the topography, such as long wavelength departures from the mean fit ellipses, and to confirm spin models. Control point solution residuals for Tethys suggest that the current spin model may be up to a degree in error. We have not addressed this problem in detail, as limb solutions for ellipsoidal objects are trivially affected by 1° errors in assumed view points (Dermott and Thomas, 1988).

Shape determination for the irregularly-shaped objects is somewhat more involved. The first step is solution of stereogrammetric control points. Such solutions require accurate spin models, which for most objects in synchronous rotation are not an issue. They are, however, an issue for Janus and Epimetheus because they swap orbits every 4 years (which induces changes in rotation periods) and have forced librations. The control point solutions were used to find the forced libration of Epimetheus and Janus (Tiscareno et al., 2009) and provided the key step in making those shape models much less uncertain than previous determinations. The control point solutions provide a network of relative three-dimensional coordinates on the surface. Limb and terminator positions help fill

E-mail address: pct2@cornell.edu

0019-1035/$ - see front matter © 2010 Elsevier Inc. All rights reserved.
doi:10.1016/j.icarus.2010.01.025

out the remainder of the shape model. Hyperion rotates chaotically and so far has been modeled separately for several flybys, or segments of flybys, in order to combine portions of shape models to generate a global one (Thomas et al., 2007b). The shape models are arrays of gridded latitude–longitude-radius values, usually at 2° or 5° spacing (also writable as triangular x, y, z coordinate sets called "plate" models). We report ellipsoidal fits to these shape models for convenience of approximate descriptions of the objects. The fit axes have been rescaled to yield a mean radius (radius of sphere of equal volume) the same as that of the actual shape model. Moments of inertia of irregularly-shaped satellites calculated from the ellipsoid axes are likely to deviate from those calculated directly from the shape model.

Uncertainties in the fit ellipsoids have been calculated based on the geographical coverage and resolution. This error estimation method seeks all possible combinations of axes that give residuals less than the minimum rms residuals increased by the expected measurement accuracy (discussed further in Thomas et al. (2007a)). These uncertainties should be considered as two-sigma values. Uncertainties in derivative quantities, such as $(a–c)$ are tabulated during the search of acceptable solutions, and do not necessarily follow directly from listed uncertainties in the individual axes.

Some simple shape and geophysical parameters are used to compare these objects to ideal, hydrostatically relaxed shapes. These parameters are derived for fluid objects (Chandrasekhar, 1969) and although idealized, apply well to bodies that effectively relax on geological time scales. "Equilibrium" shapes can involve non-fluid parameters (Holsapple, 2004), but in this work for ellipsoidal objects we refer to the fluid approximations only. The parameter $F = (b–c)/(a–c)$, where a, b, c are the Saturn-facing, orbit-facing, and polar semi-axes, is used to test for hydrostatic shape. An equilibrium F is 0.25 for moderate rotation speeds; for close, rapidly rotating satellites such as Mimas, F decreases slightly (Table 2 and Dermott and Thomas, 1988). For hydrostatic bodies, $(a–c)$ increases with lower density and higher spin rate (Chandrasekhar, 1969; Dermott, 1979), and it decreases if there is a central concentration of mass such as that resulting from differentiation. Dynamic heights (Vanicek and Krakiwsky, 1986; Thomas, 1993) are close proxies for distance above a reference equipotential surface.

The goal of this work is to update the shape information on saturnian satellites and to note changes in related interpretations. These results supersede the great majority of those in Thomas et al. (2007a) and Porco et al. (2007); comparisons are listed in Supplementary material. Dimensions of some satellites have been improved by more recent imaging that widens the geographic coverage and thereby restricts the global fit shape better than earlier solutions. Uncertainties in fit dimensions are reduced, and thus uncertainties in quantities such as mean densities are lower, and any related interpretations are improved.

2. Summary results

Tables 1–3 list the results for the ellipsoidal and irregularly-shaped satellites. Fig. 1 shows an example of how the shape results evolved with increasing numbers of images. Tethys is taken as an example because it is a moderately rough satellite and early images did not provide a good set of crossing limb tracks, which resulted in a somewhat unstable solution. The roughness of the limb affects the center-finding for each projected ellipse, with cascading effects on the three-dimensional shape solution. The spike in shape measures (8th image) occurred with the addition of a high resolution image (N1514130023) that dominated the residuals and

Table 1
Ellipsoidal satellite shapes.

Satellite	a	b	c	Mean radius	$a–c$, km	ρ, kg m^{-3}	g, cm s^{-2}	Im	Data
Mimas	207.8 ± 0.5	196.7 ± 0.5	190.6 ± 0.3	198.2 ± 0.4	17.2 ± 0.5	1149 ± 7	5.9–6.5	36	21,527
Enceladus	256.6 ± 0.3	251.4 ± 0.2	248.3 ± 0.2	252.1 ± 0.2	8.3 ± 0.3	1609 ± 5	11.0–11.4	37	25,602
Tethys	538.4 ± 0.3	528.3 ± 1.1	526.3 ± 0.6	531.0 ± 0.6	12.1 ± 0.9	985 ± 3	14.3–14.7	32	20,789
Dione	563.4 ± 0.6	561.3 ± 0.5	559.6 ± 0.4	561.4 ± 0.4	3.8 ± 0.7	1478 ± 3	22.8–23.1	45	33,229
Rhea	765.0 ± 0.7	763.1 ± 0.6	762.4 ± 0.6	763.5 ± 0.6	2.6 ± 0.9	1237 ± 3	25.9–26.2	45	34,690
Iapetus	745.7 ± 2.9[a]	745.7 ± 2.9[a]	712.1 ± 1.6	734.3 ± 2.8	33.6 ± 2.8	1088 ± 13	22.0–22.3	69	18,280

$a–c$ (all in kilometers) are the Saturn-facing, orbit-facing, and polar radii. Uncertainties are the two-sigma values of estimated accuracies as described in text.
Mean radius is the radius of a sphere of equivalent volume.
ρ, mean density, determined from masses reported in Jacobson et al. (2006).
g is surface acceleration. Range of values derives from different radii and differing tidal effects.
Im: number of images used.
Data: number of individual limb coordinates.
[a] Solution given is for an oblate spheroid fit. Triaxial fit has semi-axes of 746.1, 745.3, 712.1 km.

Table 2
Satellite equilibrium parameters.

Satellite	$a–c$, km	$(a–c)h$, km	F_{obs}	F_{pred}	$\Delta(b–c)$, km	$H\Delta dh$, km	$D\Delta dh$, km	rms, km
Mimas	17.2 ± 0.6	19.7	0.35 ± .02	0.21	2.4	1.7	1.4	0.70
Enceladus	8.3 ± 0.3	8.0	0.37 ± .04	0.23	1.1	0.5	1.2	0.44
Tethys	12.1 ± 0.9	14.7	0.17 ± .15	0.24	0.84	1.0	0.6	1.17
Dione	3.8 ± 0.7	4.9	0.45 ± .20	0.25	0.8	0.6	0.5	0.72
Rhea	2.6 ± 0.9	2.9	0.27 ± .10	0.25	0.05	0.15	0.21	1.14
Iapetus	33.6 ± 2.8	0.01	0.96 ± .03	0.25	24.1	13.9	16.4	3.65

$(a–c)h = (a–c)$ predicted for homogeneous model.
$F_{obs} = (b–c)/(a–c)$.
$F_{pred} = F$ for a homogeneous, relaxed object at the particular orbital distance.
$\Delta(b–c)$ is $(F_{obs}–F_{pred}) * (a–c)$.
$H\Delta dh$ is range of dynamic heights for homogeneous model.
$D\Delta dh$ is range of dynamic heights for differentiated model, mantle density 930 kg m^{-3} and core density 3000 kg m^{-3}.
rms is root mean square of limb fit residuals (observed – predicted radius) in kilometers for all data.

Table 3
Properties of irregularly-shaped saturnian satellites.

Satellite	a	b	c	r_m	Mass	ρ, kg m^{-3}	g, cm s^{-2}
Pan	17.2 ± 1.9	15.7 ± 1.3	10.4 ± 0.84	14.1 ± 1.3	0.495 ± .075	420 ± 150	0.01–0.18
Daphnis	4.3 ± 0.7	4.1 ± 0.9	3.2 ± 0.8	3.8 ± 0.8	0.0077 ± .0015	340 ± 260	0.01–0.04
Atlas	20.4 ± 1.2	17.7 ± 0.7	9.4 ± 0.8	15.1 ± 0.9	0.66 ± 0.045	460 ± 110	0.02–0.20
Prometheus	67.8 ± 3.1	39.7 ± 3.1	29.7 ± 1.9	43.1 ± 2.7	15.95 ± 0.15	480 ± 90	0.13–0.58
Pandora	52.0 ± 1.8	40.5 ± 2.0	32.0 ± 0.9	40.7 ± 1.5	13.71 ± 0.19	490 ± 60	0.26–0.60
Epimetheus	64.9 ± 2.0	57.0 ± 3.7	53.1 ± 0.7	58.1 ± 1.8	52.66 ± 0.06	640 ± 62	0.64–1.1
Janus	101.5 ± 1.9	92.5 ± 1.2	76.3 ± 1.2	89.5 ± 1.4	189.75 ± .0006	630 ± 30	1.1–1.7
Methone	1.6 ± 0.6	1.6 ± 0.6	1.6 ± 0.6	1.6 ± 0.6			
Pallene	2.9 ± 0.6	2.8 ± 0.8	2.0 ± 0.4	2.5 ± 0.6			
Telesto	16.3 ± 0.5	11.8 ± 0.3	10.0 ± 0.3	12.4 ± 0.4		–	
Calypso	15.1 ± 0.3	11.5 ± 2.2	7.0 ± 0.6	10.7 ± 0.7		–	
Polydeuces	1.5 ± 0.6	1.2 ± 0.4	1.0 ± 0.2	1.3 ± 0.4			
Helene	21.7 ± 0.5	19.1 ± 0.3	13.0 ± 0.3	17.6 ± 0.4			
Hyperion	180.1 ± 2.0	133.0 ± 4.5	102.7 ± 4.5	135 ± 4	561.99 ± 5	544 ± 50	1.7–2.1
Phoebe	109.4 ± 1.4	108.5 ± 0.6	101.8 ± 0.3	106.5 ± 0.7	829.2 ± 1	1638 ± 33	3.8–5.0

Masses for Janus, Epimetheus, Atlas, Prometheus, and Pandora are from Jacobson et al. (2008). Masses for Pan and Daphnis are from Porco et al. (2007). Mass of Hyperion from Thomas et al. (2007b). Mass of Phoebe is from Jacobson et al. (2006). Masses are in units of 10^{19} g.

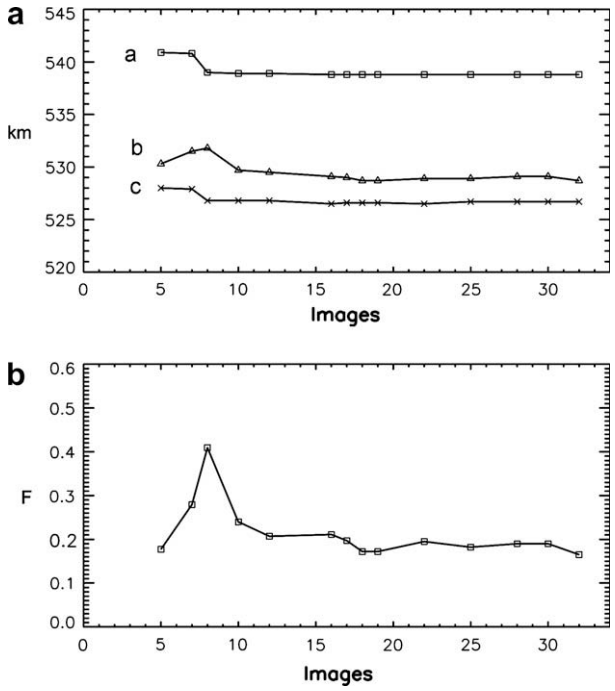

Fig. 1. Tethys axial fits as a function of increasing number of images used in solution. Tethys F value $(b–c)/(a–c)$ with increasing number of images. Images are in order in which they were added to the data set; the first four did not provide crossing tracks and gave an unstable solution.

which had slightly less than a 180° limb arc, thus pushing the solution toward the slightly off-center result for that image. Once high resolution images with somewhat more than 180° of limb arc pinned the dimension at one view, the solution did not vary much with further data. Fig. 2 shows ground tracks of limb data on all the satellites measured.

2.1. Ellipsoidal objects: summary

Previous work had suggested that all these objects at sometime had approached equilibrium shapes, wherein the surface approaches that of a fluid body shaped solely by gravity, tidal, and rotational forces (Thomas et al., 2007a). Fig. 3 illustrates the relation of the measured $(a–c)$ of the ellipsoidal satellites to that expected for hydrostatically relaxed objects of the observed mean density and mean radius with homogeneous interiors, and for differentiated models with a core density of 3000 kg m^{-3} and a mantle density of 930 kg m^{-3}. This shape parameter suggests all saturnian ellipsoidal satellites might meet some observational criteria of hydrostatic shapes for some interior model. However, the F parameters and the range of dynamic heights (Table 2), suggest limits on such interpretations. In particular, Enceladus's $(a–c)$ is best fit by a homogeneous interior model (Thomas et al., 2007a), yet the ongoing activity and relaxation of short wavelength topography are very strong geological reasons to expect that internal heating has led to a differentiated interior.

Mimas's shape might suggest interior mass concentration (Dermott and Thomas, 1988; Eluszkiewicz, 1990), but again the F parameter value limits what can be inferred using an assumption of hydrostatic equilibrium. The newer values of semi-axes of Mimas differ from the previous ones by 0.4 km or less, and the discussion in Thomas et al. (2007a) still applies: Mimas's b axis is too large for an equilibrium shape. Although Mimas is a triaxial ellipsoid, not the product of impact shaping, and approached an equilibrium form, interpreting the interior configuration from the shape is limited by this small departure from hydrostatic shape. Mimas's interior must have been highly rigid for most of its history for it to sustain a free eccentricity of ~0.02 (McKinnon and Barr, 2007), and thus maintaining a slight departure from a hydrostatic shape is reasonable.

Iapetus stands out as having a shape far from equilibrium with its current spin period (Fig. 3). Its oblate spheroid shape probably was frozen at a much shorter spin period (~16 h; Castillo-Rogez et al., 2007). Our updated shape for Iapetus is slightly different from the earlier reported values ($(a–c)$ of 33.5 km vs. previous 35.0 km, estimated uncertainty 3.6 km), but is well within the previously estimated uncertainties and invites no significant change to the conclusions of Castillo-Rogez et al. (2007).

Dione's fit axes have changed slightly (0.3–0.4 km) from those previously reported. As shown in Table 2 and Fig. 3, Dione's $(a–c)$ is smaller than the homogeneous predicted value and thus might suggest interpretation as a differentiated object (Fig. 3). However, the F parameter of 0.45 suggests that Dione may deviate enough from a hydrostatic shape that inferences on the interior may be risky as with Enceladus. The calculations of the range of dynamic heights confirms the difficulty of discriminating between interior models, as there is only a 100 m difference in dynamic height ranges between the homogeneous and differentiated models. The shape by itself suggests that the object has been close to hydrostatic equilibrium, but more detailed conclusions require higher order knowledge.

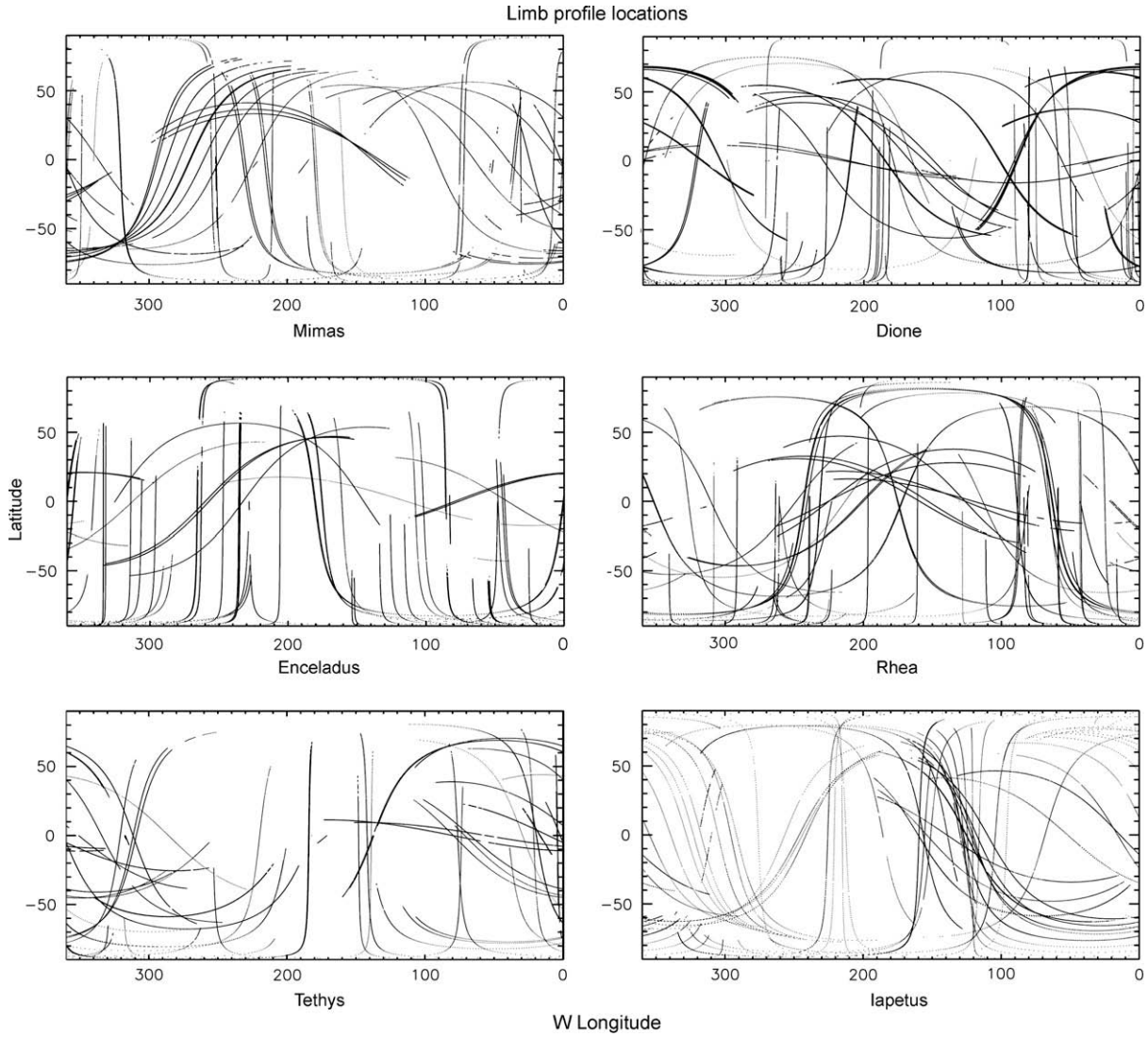

Fig. 2. Ground tracks of limb data on ellipsoidal satellites.

2.2. Ellipsoidal objects: Tethys and Rhea global shapes

Measured semi-axes for Tethys have changed from those in Thomas et al. (2007a) by 2.0, 2.8, and 1.2 km. Tethys had only seven useful images in the prior work, and subsequent data have greatly reduced the uncertainties. The measured shape of Tethys is close to hydrostatic, and the (a–c) suggests, with the caveats described above, as perhaps favoring some differentiation. The differentiated model supports less topography than the homogeneous one. However, given the roughness of the surface, and likely tectonic effects on crustal homogeneity and thickness, it is not possible to choose an interior model. The mean density of Tethys is sufficiently low that a core of density 3000 kg m^{-3} would be only ~160 km in radius. If one instead assumes a greater crust/core difference, with crustal density of 910 kg m^{-3} and a core of 3500 kg m^{-3}, the core size increases by only ~5 km.

It has not been clear if Rhea is a homogeneous or differentiated object, or whether it is in hydrostatic equilibrium (Iess et al., 2007; Anderson and Schubert, 2008; Asmar et al., 2009). Previous shape data (that used by Asmar et al. (2009)) had the c axis 0.6 km larger than the b axis, although uncertainties on each were at least this amount. The (a–c) was also nominally considerably larger than a homogeneous model would predict. As a result, the shape provided no insight into interpretations of the gravity data, such as supporting an assumption of hydrostatic equilibrium. The more complete coverage (45 images vs. previous 22, and generally somewhat higher resolution) shows a hydrostatic shape, with an (a–c) very close to the homogeneous model value, and a value of F consistent with hydrostatic equilibrium. There is no significant difference in the calculated range of dynamic heights for the differentiated and homogeneous models of Rhea. The low mean density renders effects of any mass concentration in a core small and difficult to detect at this level of accuracy. These data indicate that hydrostatic models of Rhea are appropriate, and unusual internal mass distributions are not necessary.

2.3. Ellipsoidal objects: local topography

Limb profiles, if properly oriented, can be useful in examining local and regional phenomena. Because the profiles are envelopes over the highest topography, they are most useful for examining large depressions, isolated positive relief forms, and regional trends where the ambiguity of the exact location of the limb along the line of sight is reduced or is not of a relevant scale. Tethys provides two kinds of application of limbs to "local" topography: large crater profiles and cross sections of the global tectonic feature

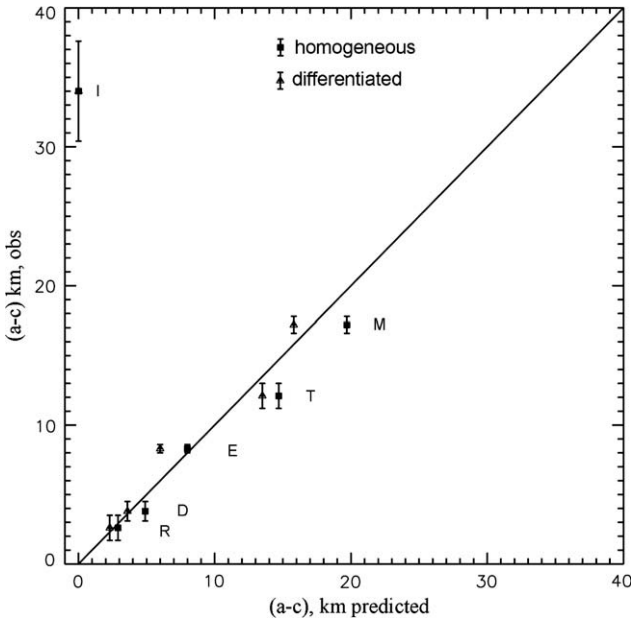

Fig. 3. Measured and predicted (a–c) for saturnian satellites. Differentiated cases assume mantle density of 930 kg m^{-3}, core density of 3000 kg m^{-3}.

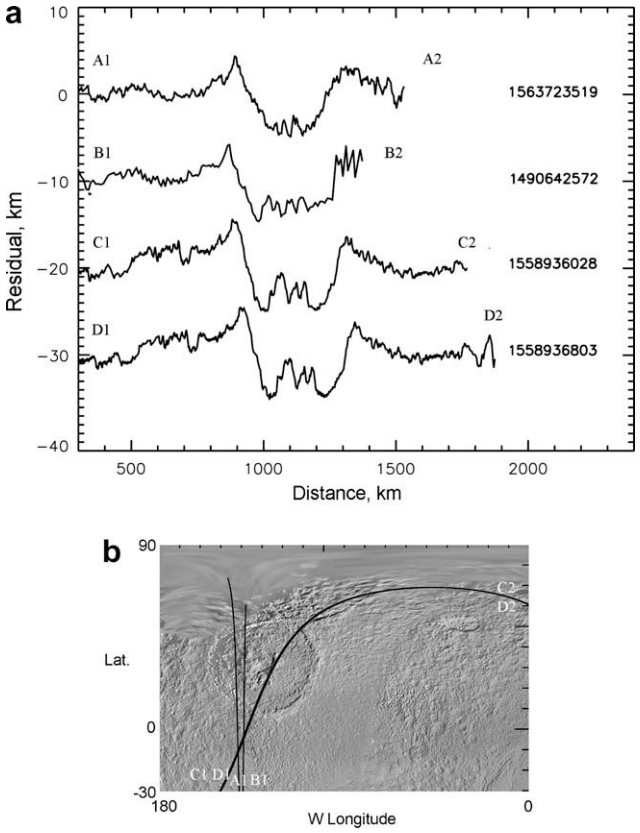

Fig. 4. Limb profiles on Odysseus crater, Tethys. (a) Portions of profiles with ISS image numbers. Residuals are the radial difference between observed limb coordinate and the limb predicted from the best ellipsoidal solution and the image geometry. (b) Predicted traces of profiles on portion of global image mosaic (mosaic from Roatsch et al. (2009)). Note profiles C and D essentially overlie one another. Vertical exaggeration is 30.

Ithaca Chasma. Odysseus crater on Tethys is over 400 km in diameter and previous work (Schenk, 1989; Moore et al., 2004) showed it to have ~8 km of relief. Limb profiles (Fig. 4) show the crater floor to reach ~6 km below the undisturbed terrain, and that Odysseus has nearly 10 km maximum relief as the rim crest rises a few km above the surroundings. Significant rim topography extends ~100 km from the rim crest.

The nearly global tectonic trough Ithaca Chasma (Fig. 5) has been investigated by terrain models derived from stereogrammetry (Giese et al., 2007); their flexure modeling concentrated on a section of the Chasma slightly north of the equator. Fig. 5 shows samples of the changing cross sections of this form at different latitudes, and emphasizes that the segment north of the equator is distinct from the narrower part south of the equator. These in turn, from the images, are only two of several morphologically distinct parts of the Ithaca Chasma system. The transition between the two sections sampled in Fig. 5 is abrupt. These variations along the trough suggest different histories and/or different mechanical properties in different parts of the crust. Such variations emphasize some of the limits of symmetric global geophysical models.

The 500-km diameter basin Engelier on Iapetus is crossed by several limb profiles (Fig. 6). These data show the depth of this feature also exceeds 10 km, with a central peak nearly 9 km in height above the crater floor reaching essentially the level of surrounding terrain. Central peaks on icy saturnian satellites can reach relative heights far larger than those in lunar craters (Dombard et al., 2007). The "background" surface is rough on the scales of 2–3 km, which prevents more detailed examination of rim-related topography.

3. Irregularly-shaped satellites

Those objects too small to relax viscously have shapes that are probably largely the result of impact effects, except for a few ring-related ones that may still include effects of accretion (Porco et al., 2007; Charnoz et al., 2007). Even for those objects that are unconsolidated and far too small to have viscous effects, mass movement and the ability of angle-of-repose effects to support topography mean objects may assume a large variety of forms (Richardson et al., 2005; Minton, 2008).

Since the compilation in Porco et al. (2007), the major advance in small satellite shapes has come through solution of the forced librations of Janus and Epimetheus (Tiscareno et al., 2009). The resulting new shape models change the mean radii of each satellite by less than 1.5 km, but some individual fit axes have changed by several kilometers. The mean densities of Janus and Epimetheus are indistinguishable (Table 3), and are good to better than 10%. The previously determined density for Epimetheus of 690 ± 130 kg m^{-3} (Porco et al., 2007) has been refined to 640 ± 30 kg m^{-3} with the better determined shape. Assuming a uniform density, the shape of Janus may imply (uncertainties in the shape allow a range of orientations) a maximum moment direction offset from the sub-Saturn orientation. Because the libration model works, the moment direction from a homogeneous model is likely in error, which would imply some internal mass inhomogeneities (Tiscareno et al., 2009).

Some fit ellipsoidal axes of Phoebe have been updated by more than a kilometer from the values in Porco et al. (2005); however, the mean radius is little changed (0.2 km). The nearly oblate spheroid shape of Phoebe may retain characteristics of an early, relaxed object. Johnson et al. (2009) noted that Phoebe's axes are close to those expected for a relaxed object of its mean density and current spin period, and that even addition of the topography expected from double the current large crater population to an initial oblate object would still on average allow a fit shape to reflect the original axial ratios. The (a–c) value for Phoebe, if it does reflect a hydrostatic equilibrium condition, is most compatible with some degree of mass concentration toward the center. Phoebe's size makes it a borderline case for viscous relaxation and/or differentiation

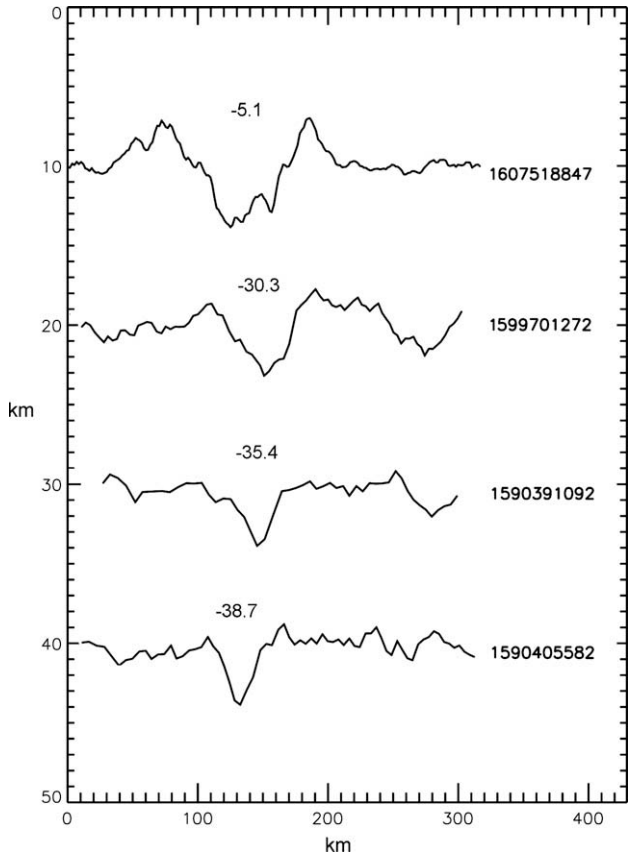

Fig. 5. Limb profiles across Ithaca Chasma. Latitudes at center of trough are given. Vertical exaggeration is 12.

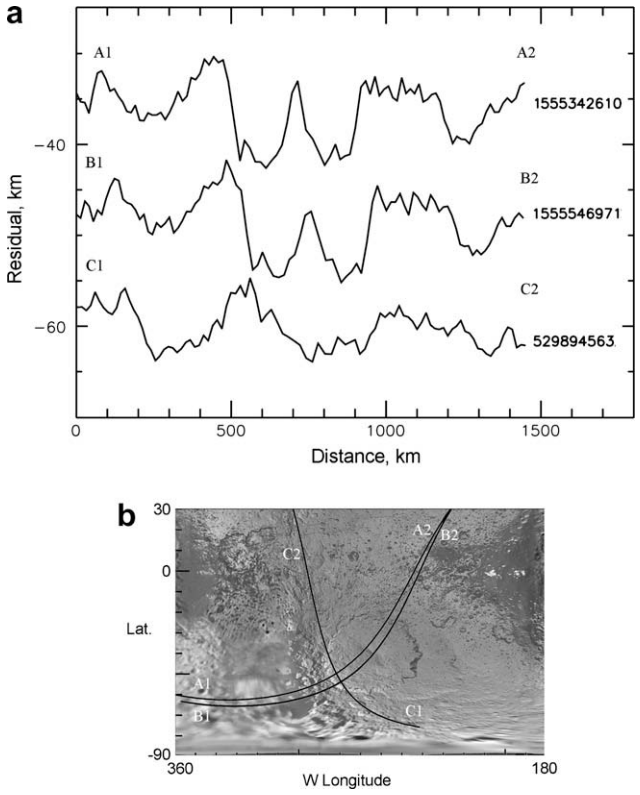

Fig. 6. Limb profile residuals across Iapetus crater Engelier. (a) Profiles with image numbers. Residuals are the radial difference between observed limb coordinate and the limb predicted from the best ellipsoidal solution and the image geometry. (b) Trace of predicted locations on portion of global image mosaic. (Image mosaic from Roatsch et al. (2009).) Top two profiles go close to center of crater, bottom one skims the western edge of the crater. Vertical exaggeration is 33.

(Johnson and McGetchin, 1973), but early formation could provide heating from ^{26}Al, and with some combinations of composition and porosity, relaxation and even differentiation might have occurred (Johnson et al., 2009).

The shapes and mean densities of some ring-related satellites may preserve attributes of their accretionary history. First, Porco et al. (2007) note that Pan, Atlas, Prometheus and Pandora nearly fill their Roche lobes, that is, very little disturbance is necessary for material to be lost from the satellite's surface into Saturn orbit. Such material would probably reaccrete and possibly follow many cycles initiated by continuing high-velocity impacts. This condition is exemplified in part by the low gravity at their long ends (Table 3). Second, Charnoz et al. (2007) noted that the equatorial ridges on Pan and Atlas match expectations of ring material accretion onto these satellites. The work here has only very slightly changed the previous shape solutions of these objects and largely emphasizes the distinction of some of the ring-related satellites from objects such as Epimetheus and Janus. The latter two objects have higher surface accelerations and smaller relative ranges of surface gravity than the ring-related objects, and have more obvious shape-modifying large craters (Table 4).

The largest craters can affect the shapes of satellites, but there is a wide range in the relative sizes of the largest craters on these objects. Table 4 lists those for which image coverage is good enough to tabulate most large craters. Epimetheus has the largest relative-sized crater, and it provides a flattened south polar region and probably determined the rotational pole position in the body. Nominally, Hyperion's largest crater should be a significant modifier of the satellite's form, but the shallow relative depth, and placement on the elongated object, means that it does not create a large concave face. The visible craters are likely the modest modifiers of shapes initiated by more catastrophic events for some of these objects. Small scale

Table 4
Largest craters on irregularly-shaped satellites.

Satellite	r_m, km	Crater diam., km	D/r_m
Pandora	40.7 ± 1.5	15.4	0.38
Epimetheus	58.1 ± 1.8	94.5	1.63
Janus	89.5 ± 1.4	52.5	0.59
Telesto	12.4 ± 0.4	8.6	0.69
Hyperion	135 ± 4	230	1.70
Phoebe	106.5 ± 0.7	100	0.94

fragmentation experiments showed most likely a/c ratios are ~2 (Fujiwara et al., 1978; Capaccioni et al., 1984), and there is a statistical suggestion from lightcurves that members of older asteroid families, presumably of fragmentation origin, become more rounded than younger ones (Szabo and Kiss, 2008). The saturnian ring-related satellites have a mean a/c of 1.81 ± 0.40 (1 s.d.; $n = 5$); others, excepting Phoebe have a mean a/c of 1.59 ± 0.31 ($n = 7$), and Mars' satellites and four inner satellites of Jupiter have a mean a/c of 1.59 ± 0.22 ($n = 6$). These comparisons may not be very meaningful due to the scaling differences between the laboratory and the satellites, and because of the impact and accumulation history of the satellites. However, most of the small saturnian satellites have shapes indistinguishable from other small objects, with the possible exceptions of ring-related ones where the real distinctions depend upon shape details, not on axial ratios.

4. Summary

Shape solutions for most of the saturnian satellites have been updated. One notable result is the determination that Rhea has a hydrostatic shape.

Acknowledgments

Brian Carcich, Karla Consroe, Sarah Morrison, Rick Kline, Pam Smith, and Paul Helfenstein provided important technical assistance. Discussions with J. Veverka, J. Burns, M. Tiscareno, and P. Nicholson were most useful. The comments from two reviewers enhanced the presentation. Funded in part by the Cassini project.

Appendix A. Supplementary material

Supplementary data associated with this article can be found, in the online version, at doi:10.1016/j.icarus.2010.01.025.

References

Anderson, J.D., Schubert, G., 2008. Rhea's gravitational field and interior structure inferred from archival data files of the 2005 Cassini flyby. Bull. Am. Astron. Soc. 40, 479.

Asmar, S.W., Nimmo, F., Thomas, P.C., Bills, B.G., 2009. A shape model for Rhea and implications for its gravity coefficients and internal structure. Lunar Planet. Sci. Conf. 40. Abstract 2219.

Capaccioni, F., Cerroni, P., Coradini, M., Farinella, P., Flamini, E., Martelli, G., Paolicchi, P., Smith, P.N., Zappala, V., 1984. Shapes of asteroids compared with fragments from hypervelocity impact experiments. Nature 309, 832–834.

Castillo-Rogez, J.C., Matson, D.L., Sotin, C., Johnson, T.V., Lunine, J.I., Thomas, P.C., 2007. Iapetus' geophysics: Rotation rate, shape, and equatorial ridge. Icarus 190, 179–202.

Chandrasekhar, S., 1969. Ellipsoidal Figures of Equilibrium. Yale Univ. Press, New Haven, 254p.

Charnoz, S., Brahic, A., Thomas, P.C., Porco, C.C., 2007. The equatorial ridges of Pan and Atlas: Terminal accretionary ornaments? Science 318, 1622–1624.

Dermott, S.F., 1979. Shapes and gravitational moments of satellites and asteroids. Icarus 37, 575–586.

Dermott, S.F., Thomas, P.C., 1988. The shape and internal structure of Mimas. Icarus 73, 25–65.

Dombard, A.J., Bray, V.J., Collins, G.S., Schenk, P.M., Turtle, E.P., 2007. Relaxation and the formation of prominent central peaks in large craters on the icy satellites of Saturn. Bull. Am. Astron. Soc. 38, 429.

Eluszkiewicz, J., 1990. Compaction and internal structure of Mimas. Icarus 84, 215–225.

Fujiwara, A., Kamimoto, G., Tsukamoto, A., 1978. Expected shape distribution of asteroids obtained from laboratory impact experiments. Nature 272, 602–603.

Giese, B., Wagner, R., Neukum, G., Helfenstein, P., Thomas, P.C., 2007. Tethys: Lithospheric thickness and heat flux from flexurally supported topography at Ithaca Chasma. Geophys. Res. Lett. 34, 1–5.

Holsapple, K.A., 2004. Equilibrium figures of spinning bodies with self-gravity. Icarus 172, 272–303.

Iess, L., Rappaport, N.J., Tortora, P., Lunine, J., Armstrong, J.W., Asmar, S.W., Somenzi, L., Zingoni, F., 2007. Gravity field and interior of Rhea from Cassini data analysis. Icarus 190, 585–593.

Jacobson, R.A., and 10 colleagues, 2006. The gravitational field of Saturn and the masses of its major satellites. Astron. J. 132, 2520–2526.

Jacobson, R.A., Spitale, J., Porco, C.C., Beurle, K., Cooper, N.J., Evans, M.W., Murray, C.D., 2008. Revised orbits of Saturn's small inner satellites. Astron. J. 135, 261–263.

Johnson, T.V., McGetchin, T.R., 1973. Topography on satellite surfaces and the shape of asteroids. Icarus 18, 612–620.

Johnson, T.V., Castillo-Rogez, J.C., Matson, D.L., Thomas, P.C., 2009. Phoebe's shape: Possible constraints on internal structure and origin. Lunar Planet. Sci. 40. Abstract 2334.

McKinnon, W.B., Barr, A.C., 2007. The Mimas Paradox Revisited Plus Crustal Spreading on Enceladus? LPI Contrib. 1357, 91–92.

Minton, D.A., 2008. The topographic limits of gravitationally bound, rotating sand piles. Icarus 195, 698–704.

Moore, J.M., Schenk, P.M., Bruesch, L.S., Asphaug, E., McKinnon, W.B., 2004. Large impact features on middle-sized icy satellites. Icarus 171, 421–443.

Porco, C.C., and 19 colleagues, 2004. Cassini Imaging Science: Instrument characteristics and anticipated scientific investigations at Saturn. Space Sci. Rev. 115, 363–497.

Porco, C.C., and 34 colleagues, 2005. Cassini Imaging Science: Initial results on Phoebe and Iapetus. Science 307, 1237–1242.

Porco, C.C., Thomas, P.C., Weiss, J.W., Richardson, D.C., 2007. Saturn's small inner satellites: Clues to their origins. Science 318, 1602–1607.

Richardson, D.C., Elankumaran, C.P., Sanderson, R.E., 2005. Numerical experiments with rubble piles: Equilibrium shapes and spins. Icarus 173, 349–361.

Roatsch, T., and 10 colleagues, 2009: High-resolution atlases of Mimas, Tethys, and Iapetus derived from Cassini-ISS images. Planet. Space Sci. 57, 83–92.

Schenk, P.M., 1989. Crater formation and modification on the icy satellites of Uranus and Saturn – Depth/diameter and central peak occurrence. J. Geophys. Res. 94, 3813–3832.

Szabo, G.M., Kiss, L.L., 2008. The shape distribution of asteroid families: Evidence for evolution driven by small impacts. Icarus 196, 135–143.

Thomas, P.C., 1993. Gravity, tides, and topography on small satellites and asteroids – Application to surface features of the martian satellites. Icarus 105, 326–334.

Thomas, P.C., Davies, M.E., Colvin, T.R., Oberst, J., Schuster, P., Neukum, G., Carr, M.H., McEwen, A., Schubert, G., Belton, M.J.S., 1998. The shape of Io from Galileo limb measurements. Icarus 135, 175–180.

Thomas, P.C., and 12 colleagues, 2007a. Shapes of the saturnian icy satellites and their significance. Icarus 190, 573–584.

Thomas, P.C., and 17 colleagues, 2007b. Hyperion's sponge-like appearance. Nature 448, 50–56.

Tiscareno, M.S., Thomas, P.C., Burns, J.A., 2009. The rotation of Janus and Epimetheus. Icarus 204, 254–261.

Vanicek, P., Krakiwsky, E.J., 1986. Geodesy: The Concepts, second ed. Elsevier, New York, 697p.